energies

MDPI

Article

A Droop Control Based Three Phase Bidirectional AC-DC Converter for More Electric Aircraft Applications

Xiancheng Zheng [1], Fei Gao [2], Husan Ali [1,*] and Huamei Liu [1]

[1] Department of Electrical Engineering, School of Automation, Northwestern Polytechnical University, Xi'an 710000, China; zxcer@nwpu.edu.cn (X.Z.); nwpu_lhm@nwpu.edu.cn (H.L.)
[2] Department of Engineering Science, University of Oxford, Oxford OX5 1PF, UK; fei.gao@eng.ox.ac.uk
* Correspondence: engr.husan@gmail.com; Tel.: +86-187-4047-6759

Academic Editor: Gabriele Grandi
Received: 20 January 2017; Accepted: 17 March 2017; Published: 20 March 2017

Abstract: This paper addresses the design and implementation of a droop controlled three phase bidirectional AC-DC converter for more electric aircraft (MEA) applications. A unified control strategy using a droop characteristic is presented to achieve the bidirectional power flow between the AC and DC source while maintaining a stable DC output voltage. Based on the rigorous control design, the converter is capable of operating over a wide frequency range with a unity power factor. The key findings obtained from the theoretical analysis are confirmed by simulation studies and further validated by a scaled down laboratory prototype. The practical results show good performance of the bidirectional converter and demonstrate the effectiveness of the proposed control strategies.

Keywords: bidirectional converter; more electric aircraft; variable frequency; droop control; *LCL*-filter

1. Introduction

The more electric aircraft (MEA) concept is one of the major trends in modern aerospace engineering which aims to reduce the overall aircraft weight, operation cost, and environmental impact [1,2].

In conventional aircraft, the flight control surfaces are activated by hydraulic actuator systems. For MEA these will be replaced by electro hydrostatic actuators (EHAs) or electromechanical actuators (EMAs) [3]. This will significantly reduce the weight of the aircraft which will improve its overall efficiency [2,4]. Thus, more electrical power is used to replace the conventional hydraulic, mechanical, and pneumatic power [5]. As a consequence, the onboard installed electrical power increases significantly and this results in challenges in the design of electrical power systems (EPS).

Generation and distribution systems constitute the main body of the MEA EPS. In recent years, electrical power generation systems have evolved from conventional constant frequency (CF) to variable speed variable frequency (VSVF) generation. This shift eliminates the mechanical gear box, increases the reliability, and reduces the maintenance cost [6]. For the distribution system, nowadays the tendency is to replace traditional AC distribution with high-voltage DC distribution [7,8]. This is because DC distribution can increase efficiency, reduce weight, and remove the need for reactive power compensation devices.

Due to the presence of both AC/DC sources in an aircraft power system and the requirement of bidirectional power flow, it is essential to have a bidirectional AC-DC power converter. Instead of the conventional Auto Transformer Rectifier Unit (ATRU), the three phase bidirectional interfaced power converter allows for tight output DC voltage control and the bidirectional power flow between AC and DC sources. In order to reduce the current harmonics for such a three phase bidirectional converter,

a high value inductor, i.e., an *L*-filter, can be installed at the AC input. However, it is bulky and not an economic solution. Instead, an *LCL*-filter can be employed due to the smaller size, lower cost, better switching ripple attenuation, and improved dynamic response [9].

In the literature, certain techniques have been discussed for the control of bidirectional power flow between AC and DC sources. Reference [10] has proposed a three phase bidirectional AC/DC converter with Y–Δ connected transformers. The converter can achieve both buck and boost AC/DC bidirectional conversion. Reference [11] proposes a modified model predictive control (MMPC) strategy based on Lyapunov function for performance improvement of a bidirectional AC-DC converter, which can be used in an energy storage system for bidirectional power flow between the three phase AC grid and energy storage devices. In reference [12] a vector decoupling controlled sinusoidal pulse width modulation (SPWM) technique has been used to maintain the constant output voltage and control the power transferred from the AC grid to the DC grid and vice-versa, with the system operating at a unity power factor. In reference [13] a three phase power converter is used to control power flow in a hybrid micro-grid. A proportional integral (PI) controller is used to stabilize the reference DC voltage by changing the reference AC side grid current which is controlled by a hysteresis controller. In all of the methods described above, the bidirectional power flow for an AC-DC converter operation has been investigated only at a single frequency. Also, none of the works described above utilize a droop control technique for bidirectional power flow.

In the literature, droop control has been widely used for load sharing among parallel sources in DC grids [14–18]. The principle of droop control in DC microgrids (MGs) is to inject a certain amount of power/current by drooping the DC voltage. Reference [14] proposes a comparative study of different droop control approaches in DC MGs with a focus on steady state power sharing and system stability. Different nonlinear voltage droops are investigated in reference [15] to analyze power flow methods for multi-terminal voltage source converter high voltage direct current (HVDC) systems. As one may know, the effect of cable impedance will affect the power sharing performance in the droop control. In reference [16], the droop gain is designed for load sharing among multiple sources in DC MGs, by including the effect of cable resistance and voltage regulation error. In reference [17], the impact of DC line impedance on the power flow of multi-terminal DC (MTDC) and the effect of the droop gain on power balancing is analyzed. In reference [18], an adaptive droop control approach is proposed in MTDC to deal with the power sharing according to the headroom (the difference between the rated capacity of the source and current loading). This proposed approach can effectively avoid the over load condition. In addition, there is a well-known tradeoff between the power sharing performance and the voltage regulation. Some improved droop control methods are proposed to reduce the voltage regulation due to the droop characteristic whilst maintaining good power sharing performance [19–21].

For MEA applications, droop control has also been successfully employed to deal with power sharing. Reference [22] presents a droop controlled twin high speed permanent magnet synchronous generators system in which appropriate power sharing between the two generators is achieved by adjusting the individual droop gain. Reference [23] proposed an improved voltage compensation method in a three source droop controlled MEA power system to effectively restore the main bus voltage. However, to the best knowledge of the authors, droop control has not been used in the bidirectional power flow control for MEA applications. To fill this gap, this paper proposes a droop characteristic to implement bidirectional power flow for a three phase AC-DC converter under variable frequency operation. Based on the presented control design, the converter can operate with variable frequency at a unity power factor and control the amount of power flow between AC and DC sources, i.e., work in rectifier and inverter mode.

The rest of the paper is organized as follows. Section 2 describes the mathematical modeling of the converter. The controller design is discussed in Section 3. Section 4 presents the simulation studies and Section 5 shows the experimental validation. Finally, the conclusions are drawn together in Section 6.

2. Mathematical Modeling of the Converter

Figure 1 shows the topology of a bidirectional three phase AC-DC converter with an *LCL*-filter. u_{dc} represents the load voltage and e_{dc} represents the DC voltage source employed for bidirectional operation. Inductor L_{dc} is added in series with the DC voltage source to prevent inrush current. $L_g - C_f - L_f$ constitutes the *LCL* filter.

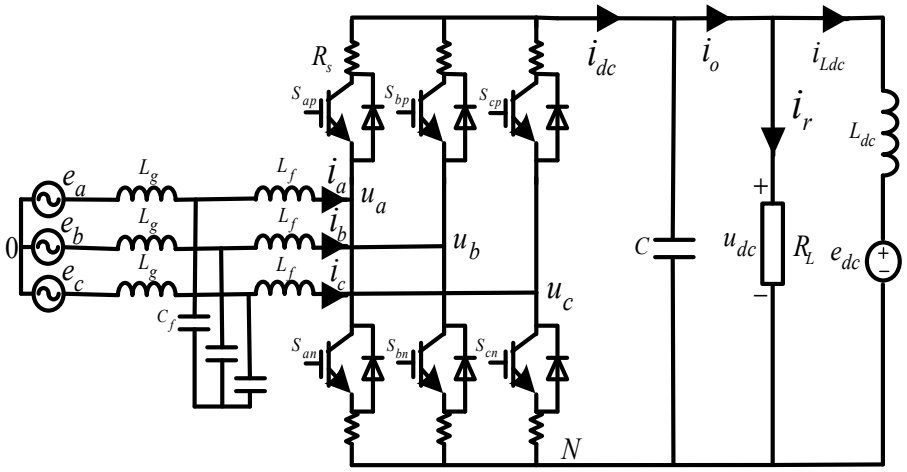

Figure 1. Topology of a three phase bidirectional AC-DC converter.

It has been shown that in the low frequency range an *LCL*-filter behaves like an *L* filter [24], where $L = L_g + L_f$. Thus, a mathematical model of the *LCL* filter in low frequency can be derived by neglecting the filter capacitor C_f [25].

2.1. Rectifier Mode

In the rectifier mode, the AC source provides the power through the bidirectional converter to DC side.

The per phase loop equation is given as:

$$L\frac{di_x}{dt} + R_s i_x = e_x - u_x = e_x - (u_{xN} + u_{N0}) \tag{1}$$

where e_x is the AC source voltage and i_x is the phase current:

$$\begin{cases} e_x = E_m \cos\left(\omega t - \frac{2\pi k}{3}\right) \\ i_x = I_m \cos\left(\omega t - \frac{2\pi k}{3}\right) \end{cases} \tag{2}$$

where $k = 0,\ 1,\ 2$ and $x = a, b, c$, respectively, and ω is the grid frequency in rad/s.

The converter side phase to neutral voltage u_{xN} and the neutral to ground voltage u_{N0} can be expressed as follows:

$$u_{xN} = u_{dc} S_x \tag{3}$$

$$u_{N0} = -\frac{u_{dc}}{3} \sum_{x=a,b,c} S_x \tag{4}$$

where S_x is the switching function.

$$S_x = \begin{cases} 1,\ S_{xp}\ is\ on\ and\ S_{xn}\ is\ off \\ 0,\ S_{xn}\ is\ on\ and\ S_{xp}\ is\ off \end{cases} \tag{5}$$

By substituting Equations (3) and (4) into Equation (1), one can obtain:

$$L\frac{di_x}{dt} + R_s i_x = e_x - u_{dc}\left(S_x - \frac{1}{3}\sum_{x=a,b,c} S_x\right) \tag{6}$$

The DC current can be expressed as a function of three phase currents:

$$i_{dc} = S_a i_a + S_b i_b + S_c i_c \tag{7}$$

A group of differential equations can be formulated in matrix form as shown in Equation (8):

$$\begin{cases} L\begin{bmatrix} \frac{di_a}{dt} \\ \frac{di_b}{dt} \\ \frac{di_c}{dt} \end{bmatrix} + R_s \begin{bmatrix} i_a \\ i_b \\ i_c \end{bmatrix} = \begin{bmatrix} e_a \\ e_b \\ e_c \end{bmatrix} - u_{dc} \begin{bmatrix} S_a - \frac{1}{3}\sum\limits_{x=a,b,c} S_x \\ S_b - \frac{1}{3}\sum\limits_{x=a,b,c} S_x \\ S_c - \frac{1}{3}\sum\limits_{x=a,b,c} S_x \end{bmatrix} \\ C\frac{du_{dc}}{dt} = [S_a,\ S_b,\ S_c]\begin{bmatrix} i_a \\ i_b \\ i_c \end{bmatrix} - \frac{u_{dc}}{R_L} - i_{Ldc} \end{cases} \tag{8}$$

Prior to the control design, the three phase stationary coordinate system is transformed into a two phase dq coordinate system using the Park transformation [12]. Thus, one can obtain:

$$\begin{cases} L\begin{bmatrix} \frac{di_d}{dt} \\ \frac{di_q}{dt} \end{bmatrix} + R_s \begin{bmatrix} i_d \\ i_q \end{bmatrix} = \begin{bmatrix} e_d \\ e_q \end{bmatrix} + \begin{bmatrix} 0 & wL \\ -wL & 0 \end{bmatrix}\begin{bmatrix} i_d \\ i_q \end{bmatrix} - \begin{bmatrix} S_d \\ S_q \end{bmatrix} u_{dc} \\ C\frac{du_{dc}}{dt} = \frac{3}{2}\begin{bmatrix} S_d & S_q \end{bmatrix}\begin{bmatrix} i_d \\ i_q \end{bmatrix} - \frac{u_{dc}}{R_L} - i_{Ldc} \end{cases} \tag{9}$$

where e_{dq} is the magnitude of the source voltage vector.

2.2. Inverter Mode

In the inverter mode, the DC source provides power to the converter and the power flows back from the DC to AC side. Thus, the differential equations in inverter mode can be formulated as follows:

$$\begin{cases} L\begin{bmatrix} \frac{di_a}{dt} \\ \frac{di_b}{dt} \\ \frac{di_c}{dt} \end{bmatrix} + R_s \begin{bmatrix} i_a \\ i_b \\ i_c \end{bmatrix} = u_{dc} \begin{bmatrix} S_a - \frac{1}{3}\sum\limits_{x=a,b,c} S_x \\ S_b - \frac{1}{3}\sum\limits_{x=a,b,c} S_x \\ S_c - \frac{1}{3}\sum\limits_{x=a,b,c} S_x \end{bmatrix} - \begin{bmatrix} e_a \\ e_b \\ e_c \end{bmatrix} \\ C\frac{du_{dc}}{dt} = -[S_a,\ S_b,\ S_c]\begin{bmatrix} i_a \\ i_b \\ i_c \end{bmatrix} - \frac{u_{dc}}{R_L} + i_{Ldc} \end{cases} \tag{10}$$

Using the Park Transformation, one can obtain:

$$\begin{cases} L\begin{bmatrix} \frac{di_d}{dt} \\ \frac{di_q}{dt} \end{bmatrix} + R_s \begin{bmatrix} i_d \\ i_q \end{bmatrix} = u_{dc}\begin{bmatrix} S_d \\ S_q \end{bmatrix} + \begin{bmatrix} 0 & wL \\ -wL & 0 \end{bmatrix}\begin{bmatrix} i_d \\ i_q \end{bmatrix} - \begin{bmatrix} e_d \\ e_q \end{bmatrix} \\ C\frac{du_{dc}}{dt} = -\frac{3}{2}\begin{bmatrix} S_d & S_q \end{bmatrix}\begin{bmatrix} i_d \\ i_q \end{bmatrix} - \frac{u_{dc}}{R_L} + i_{Ldc} \end{cases} \tag{11}$$

The equivalent representation of the system can be modeled in a synchronous reference frame (SRF), as shown in Figure 2.

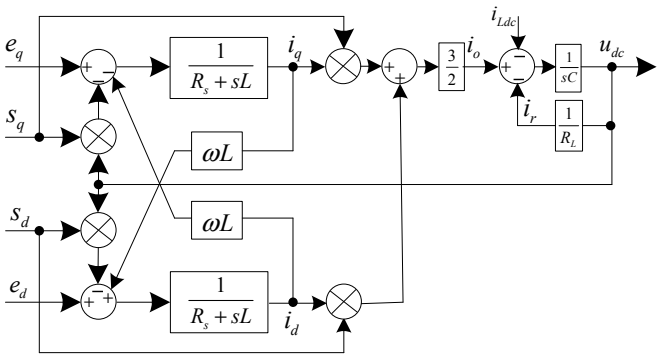

Figure 2. Modelling of the system in the *dq* frame.

3. Control Design

A droop control scheme is proposed so that the converter can work in rectifier/inverter mode using the same control strategy. Figure 3 shows the control diagram which consists of two inner current loops with decoupled dynamics and an outer DC current loop. Conventional vector control is employed. The *d*-axis is used to control the active power and the *q*-axis is used to control the reactive power independently. In order to achieve a unity power factor, the current reference in the *q*-axis i_q^* is set to zero. A SRF phase locked loop (PLL) is used to synchronize the converter frequency as well as the phase with the grid. It is worth noticing that instead of tightly regulating the voltage, the output DC current is controlled to follow the reference obtained by the droop characteristic.

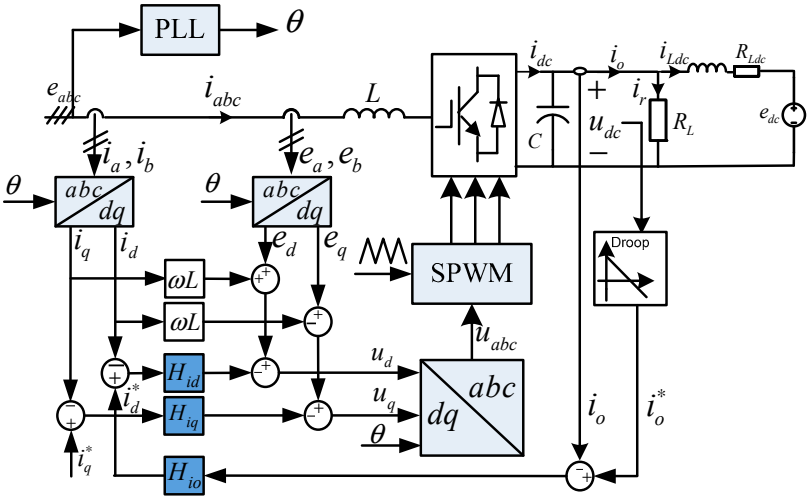

Figure 3. Unified control scheme of the three phase bidirectional converter.

3.1. Inner Current Loop

Figure 4 shows the block diagram of the inner current control loop in the *d*-axis. An equivalent diagram is valid for the *q*-axis as well.

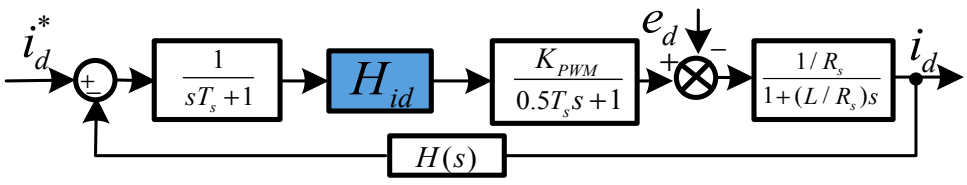

Figure 4. Inner current control loop diagram for the *d*-axis.

The computational delay of the digital controller is simulated by a first-order lag block $1/(sT_s + 1)$ where T_s is the sampling time. The switching frequency is chosen to be the same as the sampling frequency ($f_s = 20$ kHz). To simplify the analysis, the blocks having small time constants (sample & hold and PWM) are combined to become $1/(1.5T_s s + 1)$ [26]. The plant can be expressed as

$$G(s) = \frac{K_{PWM}}{(1.5T_s s + 1)(Ls + R_s)} \tag{12}$$

where K_{PWM} is the gain of the pulse width modulation (PWM). Figure 5 shows the Bode plot of the plant.

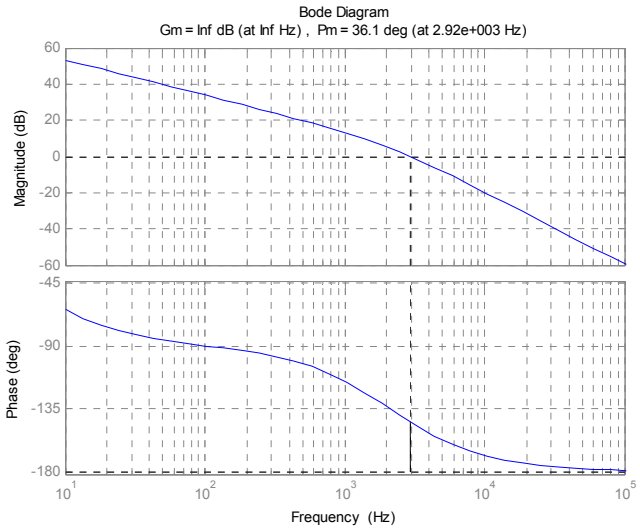

Figure 5. Bode plot of the plant.

A PI controller is utilized here to implement the closed loop control of the inner current. Then the open loop transfer function G_{io} becomes:

$$G_{io}(s) = \frac{K_{PWM}}{(1.5T_s s + 1)(Ls + R_s)} H_{id} \tag{13}$$

Substituting $H_{id} = K_{Pi} + K_{Ii}/s$ in Equation (13) one can obtain:

$$G_{io}(s) = \frac{K_{PWM}(K_{Pi} s + K_{Ii})}{(1.5T_s s + 1)(Ls + R_s)s} \tag{14}$$

To maintain the second order of the control plant after the addition of the controller, the parameters of the PI controller are chosen as expressed in Equation (15):

$$\frac{K_{Pi}}{K_{Ii}} = \frac{L}{R_s} \tag{15}$$

To design a faster inner current loop, the crossover frequency is set to be approximately one tenth of the switching frequency. The crossover frequency is the point at which the open loop gain of the system is 0 dB. Applying the criteria $20\log|G_{io}| = 0$ dB to Equation (14), one can obtain:

$$\frac{K_{Pi} K_{PWM}}{L\sqrt{(1.5T_s w_c^2)^2 + w_c^2}} = 1 \tag{16}$$

Using Equations (14) and (15), the PI controller gains can be solved as:

$$K_{Pi} = \frac{L\sqrt{(1.5T_s w_c^2)^2 + w_c^2}}{K_{PWM}},\ K_{Ii} = \frac{R_s\sqrt{(1.5T_s w_c^2)^2 + w_c^2}}{K_{PWM}} \tag{17}$$

Choosing a 2 kHz crossover frequency, the PI controller gains can be calculated and the values are listed at the end of this section. This value ensures that the bandwidth of the inner current loop is ten times smaller than the sampling frequency.

Figure 6 shows the Bode diagrams of the open loop frequency response following the above mentioned design criterion. The gain margin is infinite and phase margin is 46.7° with a stable closed loop response. It can also be seen that the PI controller is able to increase the phase margin of the plant $G(s)$ for the open loop transfer function of the inner current loop $G_{io}(s)$.

The closed loop transfer function of the inner current loop can be expressed as:

$$G_{ic} = \frac{K_{PWM}K_{Pi}}{1.5T_s Ls^2 + Ls + K_{PWM}K_{Pi}} \tag{18}$$

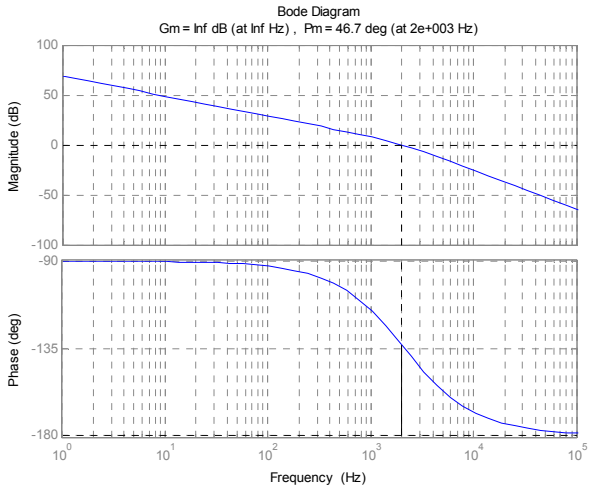

Figure 6. Bode plot of the open loop frequency response for the inner current loop.

3.2. Droop Control

As illustrated in Figure 3, the *d*-axis current reference is given by an outer DC current controller. The output DC voltage is measured and the corresponding DC current reference is generated using a droop characteristic. Figure 7 shows the detailed droop characteristic applied in this system.

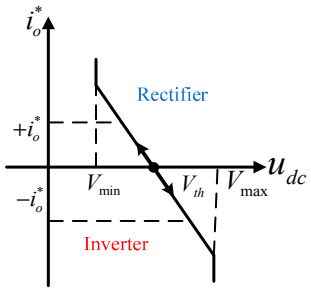

Figure 7. Droop characteristic.

At the threshold voltage V_{th}, the output current reference is set to be zero. When the output voltage is less than V_{th}, the current reference is positive, indicating that the power is flowing from AC to DC and the converter will operate in rectifier mode. In contrast, when the output voltage is

greater than the V_{th}, the current reference is negative and the converter will operate in inverter mode (power flow from DC to AC). It is worth noting that the slew rate of the droop characteristic for the rectifier and inverter mode can be different. For the sake of simplicity, in this paper the same slope, K_1, is used for both modes. Thus, the DC current reference can be expressed as:

$$i_o^* = K_1 u_{dc} + K_2 \tag{19}$$

The slew rate K_1 can be designed as a ratio of the maximal current to the maximum available voltage range, as shown in Equation (20):

$$K_1 = -\frac{I_{max}}{\Delta V_{dcmax}} \tag{20}$$

The threshold voltage V_{th} (at which the current reference is zero) can be written as:

$$V_{th} = -\frac{K_2}{K_1} \tag{21}$$

Substituting Equation (21) into Equation (20), the droop control parameter K_2 can be derived as:

$$K_2 = \frac{I_{max} V_{th}}{\Delta V_{dcmax}} \tag{22}$$

Based on this design principle, the droop control parameters K_1 and K_2 can be calculated and are listed in Table 1.

Table 1. Control Parameters.

Category	Symbols	Parameters
Inner current controller	H_{ic}	K_{pi} = 0.553 Ω, K_{Ii} = 17.27 Ω·s^{-1}
Outer current controller	H_{io}	K_{pv} = 0.45, K_{Iv} = 40 s^{-1}
Droop controller	K_1	−4 A/V
Droop controller	K_2	1608.89 A

3.3. Outer DC Current Loop

After the droop controller is designed, the DC current is regulated via a PI controller to follow the reference obtained from the droop characteristic. Figure 8 shows the control block diagram of the outer current loop. H_{io} is the DC current controller, G_{ic} is the closed loop transfer function of the inner current control loop (see Equation (18)), and $G_{i_{dc}i_o}$ is the transfer function of the ratio between i_{dc} and i_o.

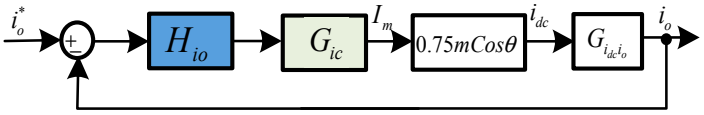

Figure 8. Outer current control loop diagram for the *d*-axis.

The relationship between the output DC current i_{dc} and the phase current magnitude I_m can be derived as shown below.

First, the DC current can be expressed as follows:

$$i_{dc} = \sum s_x i_x, \; x = a, b, c \tag{23}$$

In order to simplify the analysis by ignoring the high frequency operation of the switching function given in Equation (5), the switching function can be rewritten as:

$$s_x \approx 0.5m\cos\left(\omega t - \theta - \frac{2\pi k}{3}\right) + 0.5 \tag{24}$$

where θ is the output of the PLL and m is the modulation index of the PWM signals.

Combining Equations (2), (23), and (24), one can obtain the following relation:

$$i_{dc} \approx 0.75 m I_m \cos\ \theta \tag{25}$$

Assuming that the converter is not over modulated ($m \leq 1$), and using the peak convention for the reference frame transformation, i_{dc} can be simplified as:

$$i_{dc} \approx 0.75 I_m \tag{26}$$

Figure 9 shows the DC side equivalent circuit in order to derive the transfer function $G_{i_{dc}i_o}$. The following differential equations can be derived from Figure 9:

$$\begin{cases} i_{dc} = i_o + C\frac{du_{dc}}{dt} \\ L_{dc}\frac{d_{i_L}}{dt} + i_L R_{Ldc} = u_{dc} - e_{dc} \\ i_o = i_L + \frac{u_{dc}}{R_L} \end{cases} \tag{27}$$

Reformatting Equation (26) yields:

$$G_{i_{dc}i_o} = \frac{i_o}{i_{dc}} = \frac{L_{dc}s + R_L + R_{Ldc}}{L_{dc}CR_L s^2 + (CR_L R_{Ldc} + L_{dc})s + R_L + R_{Ldc}} \tag{28}$$

From Figure 8, the plant of the outer DC current loop is given as:

$$G_{oc} = 0.75 G_{i_c} G_{i_{dc}i_o} \tag{29}$$

Similar to the control design of the inner current loop, a PI controller H_{io} is selected using Matlab SISOTOOL (R2016a, MathWorks, Natick, MA, USA) and the values are listed in Table 1. Figure 10 shows the Bode plot of the open loop frequency response for the outer current loop.

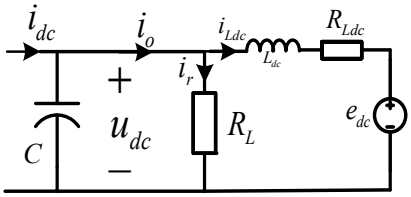

Figure 9. $G_{i_{dc}i_o}$ transfer function derivation.

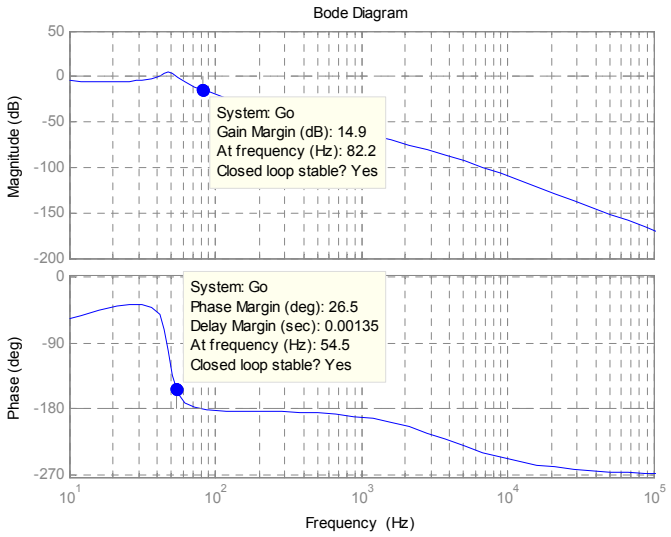

Figure 10. Bode plot of the open loop frequency response for the outer current loop.

4. Simulation Studies

The simulation studies were conducted using the power electronics system simulation program SABER to support the discussion above. The parameter selection of the *LCL*-filter has been widely discussed in the literature. Following the procedure given in [24], the *LCL*-filter in this work was designed and is listed in Table 2. The resonant frequency can be calculated as follows:

$$f_{res} = \frac{1}{2\pi}\sqrt{\frac{L_g + L_f}{L_g L_f C_f}} = 9760 \text{ Hz} \tag{30}$$

Since the variable frequency f ranges from 360 Hz to 800 Hz, the resonant frequency is within the limit $[10f,\ 0.5f_{sw}]$ which avoids the resonance problems over the harmonic spectrum.

To maintain coherence with the theoretical analysis, the simulation parameters for the bidirectional AC-DC converter are given in Table 2. In this section, the converter has been tested for variable frequency operation and bidirectional power flow.

Table 2. Simulation Parameters.

Parameter	Symbols	Value
Input AC voltage	V_{ac}	115 V_{rms}
Source frequency	f	360–800 Hz
Grid side inductor	L_g	0.26 mH
Converter side inductor	L_f	0.18 mH
Filter capacitor	C_f	2.5 µF
IGBT Resistance	R_s	0.01 Ω
Switching frequency	f_{sw}	20 kHz
PWM gain	K_{pwm}	10
DC link capacitor	C	3000 µF
Nominal voltage	V_{dc}	400 V
DC source voltage	e_{dc}	380–420 V
Threshold voltage	V_{th}	402 V
DC source series inductance	L_{dc}	3.6 mH

4.1. Variable Frequency Operation

The bidirectional AC-DC converter was simulated over a range of variable frequencies in both rectifier and inverter mode. A variable frequency AC power supply is used to mimic the output of the generator.

Figure 11 shows the simulation result of the bidirectional converter working in the frequency range of 360–700 Hz in the rectifier mode. It can be clearly seen that the drawn AC current is in phase with the grid voltage, indicating a unity power factor operation. Also, it demonstrates the effectiveness of the decoupling control strategy described in Section 2.

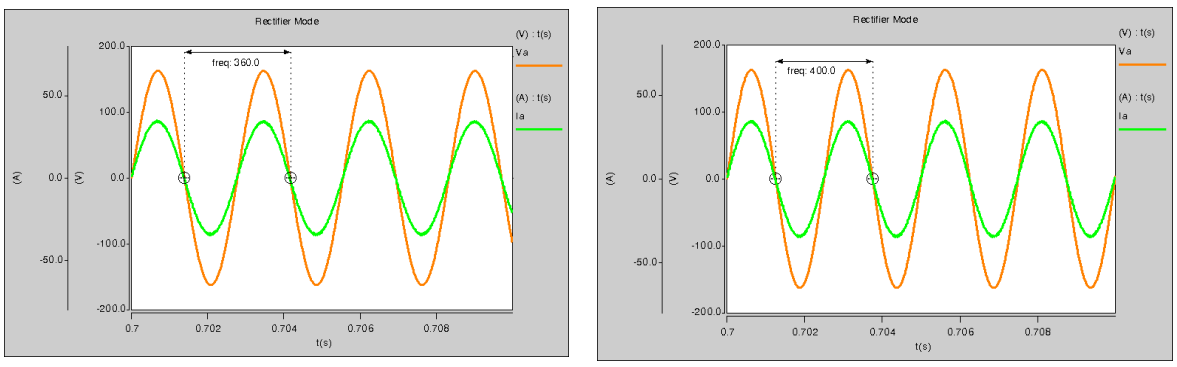

(**a**) (**b**)

Figure 11. *Cont.*

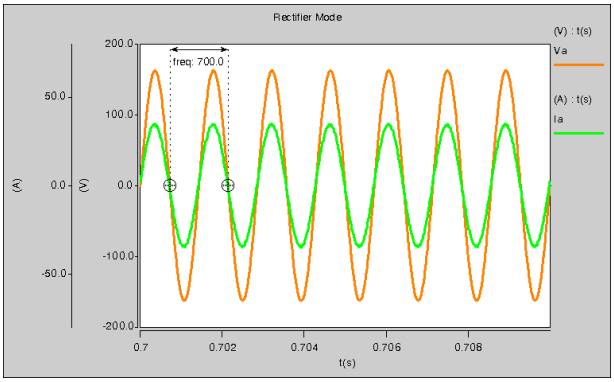

(**c**)

Figure 11. Variable frequency operation in rectifier mode (**a**) 360 Hz; (**b**) 400 Hz; and (**c**) 700 Hz.

Figure 12 shows the simulation result when the converter operates in inverter mode. It can be observed that the AC current is out of phase with the AC voltage, indicating that the power is flowing from the DC to AC source.

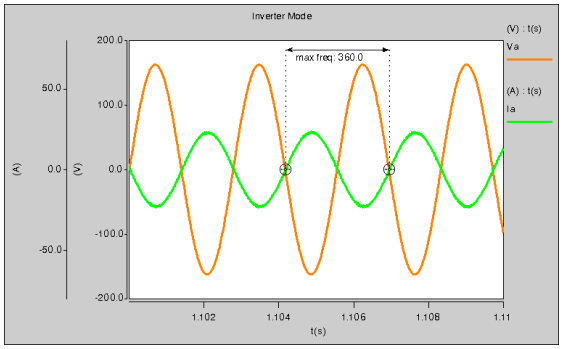

(**a**)

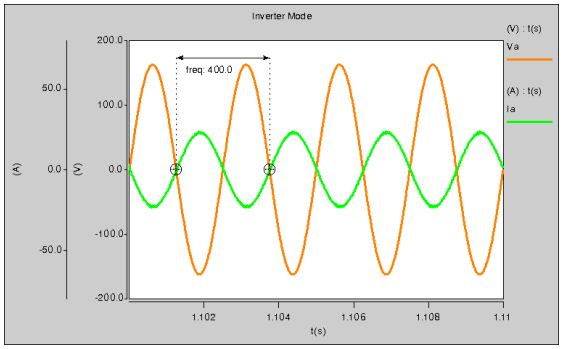

(**b**)

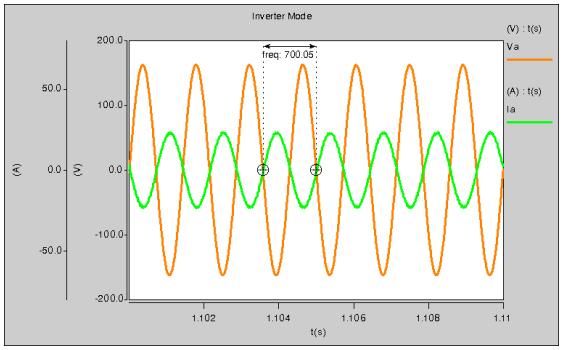

(**c**)

Figure 12. Variable frequncy operation in inverter mode (**a**) 360 Hz; (**b**) 400 Hz; and (**c**) 700 Hz.

4.2. Change of the Working Mode

Following the discussion in Section 3, the bidirectional converter allows the power to flow in either direction by using the presented unified control scheme. When the DC source voltage is less than or equal to the threshold voltage, the reference current is positive and the converter will be operating in rectifier mode. In contrast, when the DC source voltage exceeds the threshold voltage, the current reference becomes negative and the converter will operate in inverter mode.

Figure 13a shows the simulation result when the converter switches from rectifier to inverter mode. At t = 1.5 s, the DC source voltage is adjusted to 405 V which exceeds the threshold value (402 V).

It can be seen that the output current I_o gradually changes from 4.9 A to −10.9 A. The steady-state DC voltage and current is consistent with Equation (18) which validates the performance of the proposed droop controller. It is also observable that the AC current is changed to be out of phase with the voltage, indicating that the power flow direction is reversed.

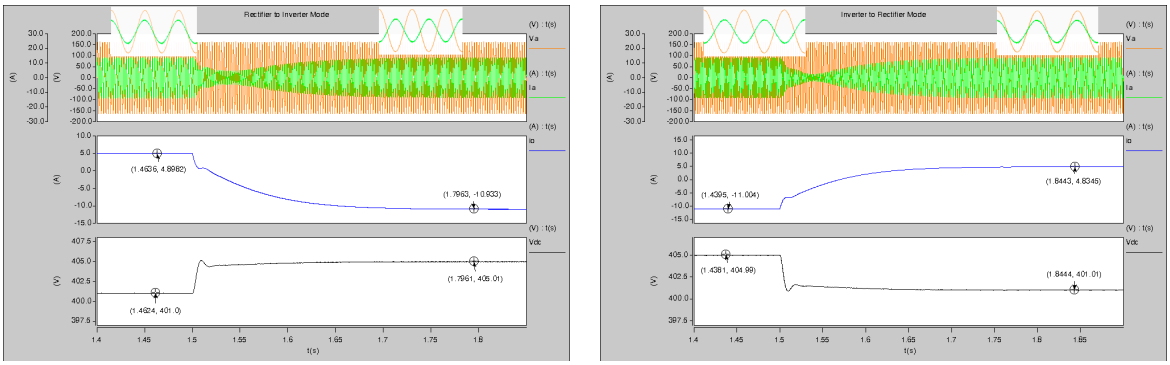

(a) (b)

Figure 13. Bidirectional power flow (**a**) rectifier to inverter mode; and (**b**) inverter to rectifier mode.

In contrast, Figure 13b shows the result when the converter operation switches its state from inverter to rectifier mode. The voltage reduces from 405 V to 401 V and the output DC current changes from −11 A to 4.83 A, indicating the change of the power flow direction. Again, the steady-state values match the designed droop characteristic in Section 3.2.

Figure 14 shows the simulation result of the converter when the DC source voltage changes. It can be seen that it follows the designed droop characteristic in Section 3.2.

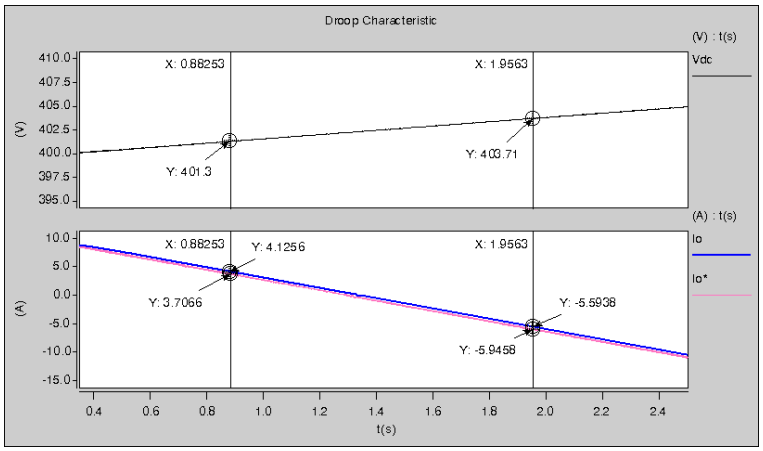

Figure 14. Droop characteristics.

4.3. Robustness Analysis

In order to perform the robustness analysis of the system, three filter inductors L and parasitic resistance R_s are varied for twenty values (5% of the nominal value). Figure 15 shows the response of the input AC current and output DC current for all the variations of the inductor and resistor. It can be clearly seen that despite the variation, the input AC current and output DC current maintain their nominal values.

In order to verify the performance of the designed controller, the resistive load (R_L) is changed at t = 1 s from 45 Ω to 75 Ω. Figure 16 shows the step response of the output voltage (u_{dc}). It can be seen that the designed control system is quite effective at countering the effect of this applied disturbance

and recovers quickly to its steady state value. The settling time is 0.01834 s. This is consistent with the designed frequency (54.5 Hz), as indicated by the crossover frequency for the open loop frequency response of the outer current loop.

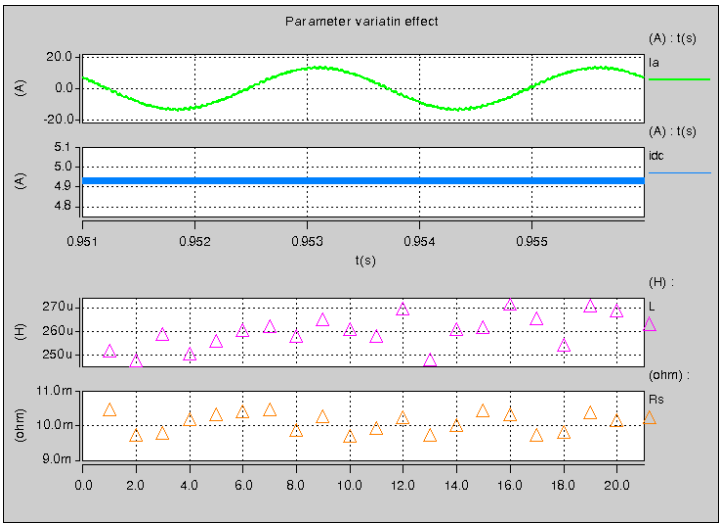

Figure 15. Parameter variation for the robustness analysis.

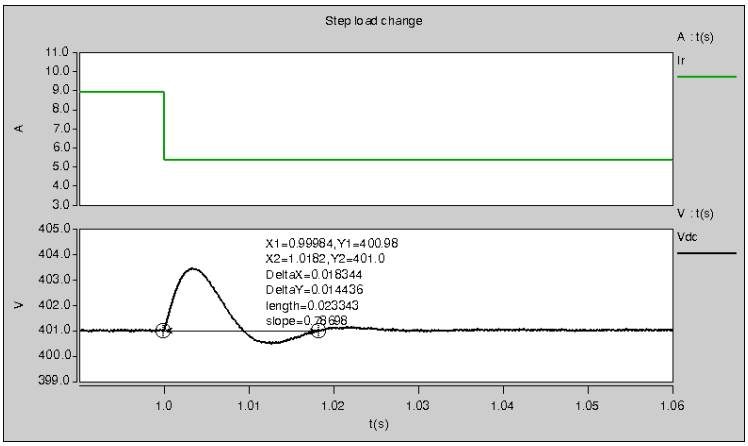

Figure 16. Step load change for the control system verification.

5. Experimental Results

In order to verify the theoretical analysis, a scaled down 2 kW prototype was designed and built in the laboratory. The control scheme (see Figure 3) has been implemented on a TMS320F2812 DSP based control platform. The experimental parameters are listed in Table 3.

Table 3. Parameters for the Prototype Bidirectional Converter.

Parameter	Symbols	Value
Input AC voltage	V_{ac}	77 V_{RMS}
Nominal voltage	V_{dc}	273.5 V
Power	P	2 kW
DC source voltage	e_{dc}	270–280 V
Threshold voltage	V_{th}	275 V
Droop characteristic	K_1	−4
Droop characteristic	K_2	1100

5.1. Variable Frequency Operation

Firstly, the laboratory prototype was tested for variable frequency operation. Figures 17 and 18 show the experimental results when the converter operates in rectifier mode and inverter mode, respectively. It can be seen that the phase current and voltage are in phase with each other in rectifier mode, and are out of phase with each other in inverter mode. The results demonstrate the unity power factor operation and confirm the effectiveness of the decoupling control.

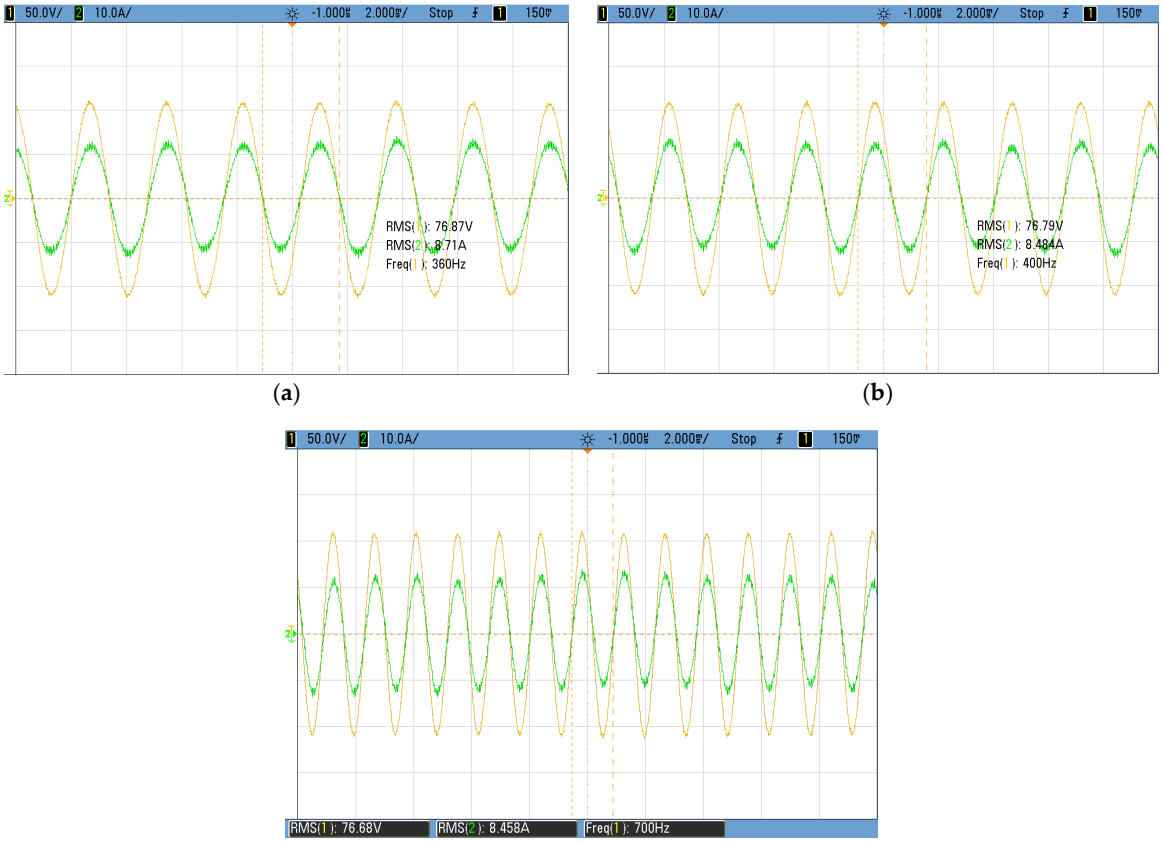

Figure 17. Variable frequncy operation in rectifier mode (**a**) 360 Hz; (**b**) 400 Hz; and (**c**) 700 Hz.

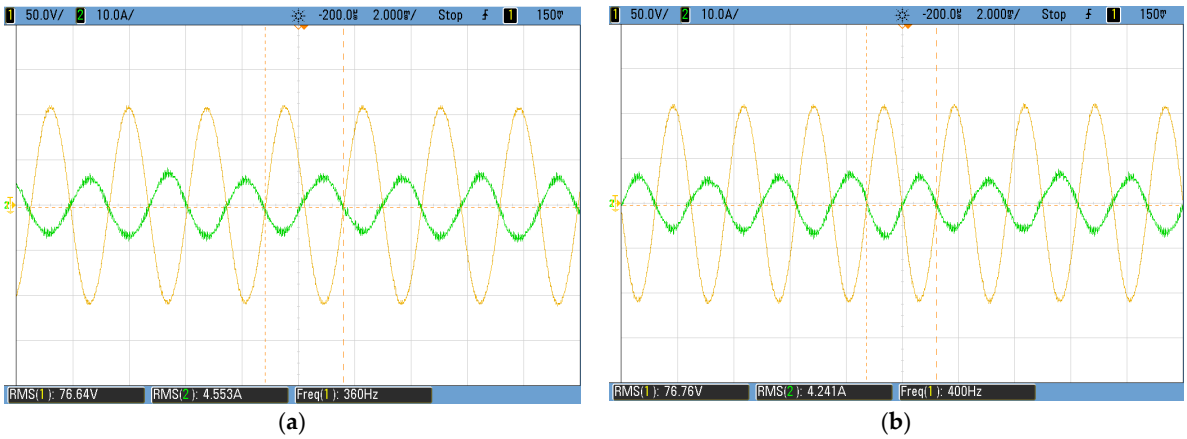

Figure 18. *Cont.*

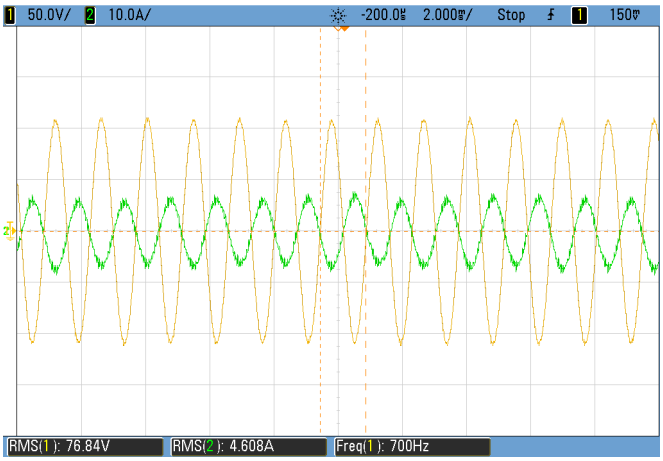

(**c**)

Figure 18. Variable frequency operation in inverter mode (**a**) 360 Hz; (**b**) 400 Hz; and (**c**) 700 Hz.

5.2. Change of the Working Mode

The prototype is also tested for the bidirectional power flow using the proposed droop control method. Figure 19a shows the experimental results of when the converter switches from rectifier to inverter mode. Successful reversal is clearly shown from the phase current and DC output current. The DC output current changes from 1.5 A to −4 A. Figure 19b presents the results of when the converter transitions from inverter to rectifier mode.

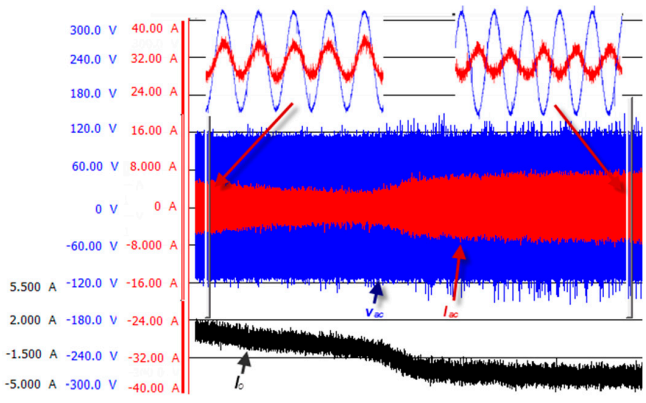

(**a**)

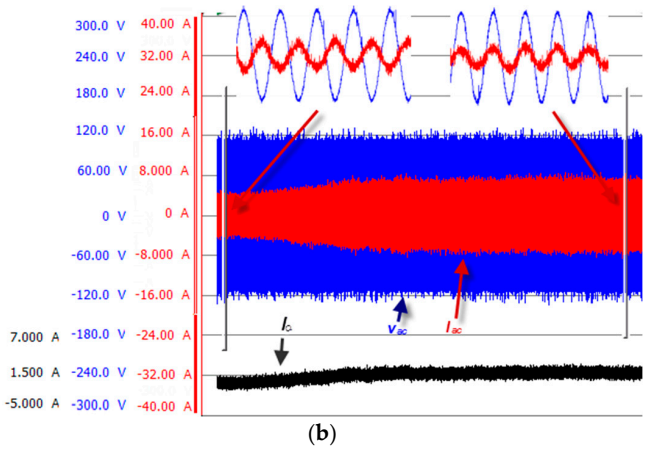

(**b**)

Figure 19. Change of the working mode (**a**) rectifier to inverter and (**b**) inverter to rectifier.

6. Conclusions

The trend in the MEA to move from traditional power sources to electrical power requires electrical systems to be redesigned considering variable frequency generation. This work has investigated a fully controlled three phase bidirectional AC-DC converter for future MEA applications. The main achievements of this work can be summarized as follows:

(1) Unity power factor operation of the converter is performed under variable frequency input.
(2) A unified control strategy is proposed for both rectifier/inverter modes. Rigorous control design of the *LCL* filter-based bidirectional converter is presented.
(3) A droop characteristic is implemented to control the bidirectional power flow between the AC and DC sources.

The simulation and experimental results demonstrate good performance of the designed bidirectional converter and the effectiveness of the bidirectional power flow using the proposed droop characteristic. Overall, this paper provides a guideline to design a bidirectional AC-DC converter for future MEA applications. The proposed method can also be applied in a multiple converter system to implement power flow regulation.

Acknowledgments: The authors would like to thank Gwilym Jones for his proofreading and English correction of the paper.

Author Contributions: Xiancheng Zheng developed the topic, reviewed and supervised the whole paper. Husan Ali and Huamei Liu performed the experiments and analyzed the data. Husan Ali wrote the paper draft. Fei Gao significantly modified the paper and provided technical feedback throughout the research.

Conflicts of Interest: The authors declare no conflict of interest.

References

1. Tariq, M.; Maswood, A.I.; Gajanayake, C.J.; Ooi, G.H.P.; Chatterjee, P.; Madishetti, S.; Molligoda, D.A.; Gupta, A.K. Battery integration with more electric aircraft DC distribution network using phase shifted high power bidirectional DC-DC converter. In Proceedings of the 2015 IEEE PES Asia-Pacific Power and Energy Engineering Conference (APPEEC), Brisbane, Australia, 15–18 November 2015.
2. Rosero, J.A.; Ortega, J.A.; Aldabas, E.; Romeral, L. Moving towards a more electric aircraft. *IEEE Aerosp. Electron. Syst. Mag.* **2007**, *22*, 3–9. [CrossRef]
3. Hartmann, M.; Miniboeck, J.; Ertl, H.; Kolar, J.W. A three-phase delta switch rectifier for use in modern aircraft. *IEEE Trans. Ind. Electron.* **2012**, *59*, 3635–3647. [CrossRef]
4. Schroter, T.; Schulz, D. The electrical aircraft network—Benefits and drawbacks of modifications. *IEEE Trans. Aerosp. Electron. Syst.* **2013**, *49*, 189–200. [CrossRef]
5. Deng, Y.; Foo, S.Y.; Bhattacharya, I. Regenerative electric power for more electric aircraft. In Proceedings of the IEEE SOUTHEASTCON, Lexington, KY, USA, 13–16 March 2014.
6. Wheeler, P.; Bozhko, S. The more electric aircraft: Technology and challenge. *IEEE Electr. Mag.* **2014**, *2*, 6–12. [CrossRef]
7. Guerrero, J.M.; Vasquez, J.C.; Matas, J.; Vicuña, L.G.; Castilla, M. Hierarchical control of droop-controlled AC and DC microgrids—A general approach toward standardization. *IEEE Trans. Ind. Electron.* **2011**, *58*, 158–172. [CrossRef]
8. Dragicevic, T.; Guerrero, J.M.; Vasquez, J.C.; Skrlec, D. Supervisory control of an adaptive-droop regulated DC microgrid with battery management capability. *IEEE Trans. Power Electron.* **2014**, *29*, 695–706. [CrossRef]
9. Bahrani, B.; Vasiladiotis, M.; Rufer, A. High-order vector control of grid-connected voltage-source converters with LCL-filters. *IEEE Trans. Ind. Electron.* **2014**, *61*, 2767–2775. [CrossRef]
10. Gu, L.; Jin, J. A three-phase bidirectional AC-DC converter with Y–Δ connected transformers. *IEEE Trans. Power Electron.* **2016**, *31*, 8115–8125.
11. Akter, M.P.; Mekhilef, S.; Tan, N.M.L.; Akagi, H. Modified model predictive control of a bidirectional AC-DC converter based on lyapunov function for energy storage systems. *IEEE Trans. Ind. Electron.* **2016**, *63*, 704–715. [CrossRef]

12. Mohamed, A.; Elshaer, M.; Mohammed, O. Bi-directional AC-DC/DC-AC converter for power sharing of hybrid AC/DC systems. In Proceedings of the IEEE Power and Energy Society General Meeting, Detroit, MI, USA, 24–29 July 2011.
13. Nassef, M.I.; Ashour, H.A.; Desouki, H. Battery-less hybrid micro-grid power management using bi-directional three phase power converter. In Proceedings of the IEEE 1st International Conference on DC Microgrids (ICDCM), Atlanta, GA, USA, 7–10 June 2015.
14. Gao, F.; Bozhko, S.; Costabeber, A.; Patel, C.; Wheeler, P.; Hill, C.I.; Asher, G. Comparative stability analysis of droop control approaches in voltage-source-converter-based DC microgrids. *IEEE Trans. Power Electron.* **2017**, *32*, 2395–2415. [CrossRef]
15. Wang, W.; Barnes, M. Power flow algorithms for multi-terminal VSC-HVDC with droop control. *IEEE Trans. Power Syst.* **2014**, *29*, 1721–1730. [CrossRef]
16. Chen, F.; Zhang, W.; Burgos, R.; Boroyevich, D. Droop voltage range design in DC micro-grids considering cable resistance. In Proceedings of the IEEE Energy Conversion Congress and Exposition (ECCE), Pittsburgh, PA, USA, 14–18 September 2014.
17. Haileselassie, T.M.; Uhlen, K. Impact of DC line voltage drops on power flow of MTDC using droop control. *IEEE Trans. Power Syst.* **2012**, *27*, 1441–1449. [CrossRef]
18. Chaudhuri, N.R.; Chaudhuri, B. Adaptive droop control for effective power sharing in Multi-Terminal DC (MTDC) grids. *IEEE Trans. Power Syst.* **2013**, *28*, 21–29. [CrossRef]
19. Lu, X.; Guerrero, J.M.; Sun, K.; Vasquez, J.C. An improved droop control method for DC microgrids based on low bandwidth communication with dc bus voltage restoration and enhanced current sharing accuracy. *IEEE Trans. Power Electron.* **2014**, *29*, 1800–1812. [CrossRef]
20. Anand, S.; Fernandes, B.G.; Guerrero, J.M. Distributed control to ensure proportional load sharing and improve voltage regulation in low voltage DC microgrids. *IEEE Trans. Power Electron.* **2013**, *28*, 1900–1913. [CrossRef]
21. Wang, P.; Lu, X.; Yang, X.; Wang, W.; Xu, D.G. An improved distributed secondary control method for DC microgrids with enhanced dynamic current sharing performance. *IEEE Trans. Power Electron.* **2016**, *31*, 6658–6673. [CrossRef]
22. Gao, F.; Bozhko, S.; Asher, G.; Wheeler, P.; Patel, C. An improved voltage compensation approach in a droop-controlled DC power system for the more electric aircraft. *IEEE Trans. Power Electron.* **2016**, *31*, 7369–7383. [CrossRef]
23. Zheng, X.; Gao, F.; Bozhko, S. *Stability Study of DC Electric Power System with Paralleled Generators for More-Electric Aircraft*; SAE Technical Paper 2014-01-2114; SAE International: Warrendale, PA, USA, 2014.
24. Liserre, M.; Blaabjerg, F.; Hansen, S. Design and control of an LCL-filter-based three-phase active rectifier. *IEEE Trans. Ind. Appl.* **2005**, *41*, 1281–1291. [CrossRef]
25. Liserre, M.; Dell'Aquila, A.; Blaabjerg, F. Stability improvements of an LCL-filter based three-phase active rectifier. In Proceedings of the IEEE 33rd Annual Power Electronics Specialists Conference (PESC), Cairns, Australia, 23–27 June 2002.
26. Mohamed, A.; Nejadpak, A.; Mohammed, O. LCL-filter-based bi-directional converter for connectivity of microgrids involving sustainable energy sources. In Proceedings of the North American Power Symposium (NAPS), Champaign, IL, USA, 9–11 September 2012.